Atmos. Chem. Phys. Discuss., https://doi.org/10.5194/acp-2018-780
Manuscript under review for journal Atmos. Chem. Phys.
Discussion started: 30 August 2018

Atmospheric Chemistry and Physics
Open Access
Discussions

Core and margin in warm convective clouds. Part I: core types and evolution during a cloud's lifetime

[1]Reuven H. Heiblum, [1]Lital Pinto, [1]Orit Altaratz, [1]Guy Dagan, [1]Ilan Koren

[1]Department of Earth and Planetary Sciences, Weizmann Institute of Science, Rehovot, Israel

Corresponding Email – ilan.koren@weizmann.ac.il

Atmos. Chem. Phys. Discuss., https://doi.org/10.5194/acp-2018-780
Manuscript under review for journal Atmos. Chem. Phys.
Discussion started: 30 August 2018

Abstract:

The properties of a warm convective cloud are determined by the competition between the growth and dissipation processes occurring within it. One way to observe and follow this competition is by partitioning the cloud to core and margin regions. Here we look at three core definitions: positive vertical velocity (W_{core}), supersaturation (RH_{core}), and positive buoyancy (B_{core}), and follow their evolution throughout the lifetime of warm convective clouds.

We show that the different core types tend to be proper subsets of one another in the following order: $B_{core} \subseteq RH_{core} \subseteq W_{core}$. Using single cloud and cloud field simulations, we find that this property is generally maintained during the growing and mature stages of a cloud's lifetime, but can break down during the dissipation stage. The cloud and its cores are centered at a similar location, while during dissipation the cores may reside at the cloud periphery.

A theoretical model is developed, showing that in both the adiabatic and non-adiabatic cases, B_{core} can be expected to be the smallest core, due to two main reasons: i) entrainment rapidly decreases the buoyancy core compared to the other core types, and ii) convective clouds may exist while being completely negatively buoyant (while maintaining positive vertical velocity and supersaturation).

Atmos. Chem. Phys. Discuss., https://doi.org/10.5194/acp-2018-780
Manuscript under review for journal Atmos. Chem. Phys.
Discussion started: 30 August 2018

Atmospheric Chemistry and Physics
Discussions

1. Introduction

Clouds are important players in the climate system (Trenberth et al., 2009), and currently constitute one of the largest uncertainties in climate and climate change research (IPCC, 2013). One of the reasons for this large uncertainty is the complexity created by opposing processes that occur at the same time but in different locations within a cloud. Although a cloud is generally considered as a single entity, physically, it can be partitioned to two main regions: i) a core region, where mainly cloud growth processes occur, and ii) a margin region, where cloud suppression processes occur. Changes in thermodynamic or microphysical (aerosol) conditions impact the processes in both regions (sometimes in different ways), and thus the resultant total cloud properties (Dagan et al., 2015). To better understand cloud properties and their evolution in time, it is necessary to understand the interplay between physical processes within the core and margin regions (and the way they are affected by perturbations in the environmental conditions).

Considering convective clouds, there are several parameters that are commonly used for separating a cloud's core from its margins (will be referred to as physical cores hereafter). Cloud buoyancy (which is the driving force for convection) is one of the intuitive parameters used and can be approximated by the following formula:

$$B = g \cdot \left(\frac{\theta'}{\theta_o} + 0.61 q_v' - LWC\right) \quad (1),$$

Where θ_o represents the reference state potential temperature, q_v is the water vapor mixing ratio, and LWC is the liquid water content. The (') stands for the deviation from the reference state per height (Wang et al., 2009).

The vertical velocity (w) and the supersaturation (S, where S=1 is 100% relative humidity) are also commonly used for defining a cloud core, and are linked as follows:

$$\frac{dS}{dt} = Q_1 w - Q_2 \frac{dLWC}{dt} \quad (2),$$

where Q_1,Q_2 are thermodynamic factors (Rogers and Yau, 1989). The thermodynamic factors are nearly insensitive to pressure for temperature above 0^oC, and both weakly decrease (less than 15% net change) with temperature increase between 0^oC and 30^oC

Atmos. Chem. Phys. Discuss., https://doi.org/10.5194/acp-2018-780
Manuscript under review for journal Atmos. Chem. Phys.
Discussion started: 30 August 2018

(Pinsky et al., 2012). The first term on the right-hand side is related to the change in the supersaturation due to adiabatic cooling or heating of the moist air (due to vertical motion). The second term is related to the change in the supersaturation due to condensation/evaporation of water vapor/drops. Hence, the supersaturation in a rising parcel depends on the magnitude of the updraft and on the condensation rate of vapor to drops (a sink term).

Previous works have used these objective measures to define a cloud core (with the margins defined as the remaining regions of the cloud). In deep convective cloud simulations the core is usually defined by the updrafts' magnitude using a certain threshold, usually $W>1\ \mathrm{m\cdot s^{-1}}$ (Khairoutdinov et al., 2009;Lebo and Seinfeld, 2011;Morrison, 2012;Kumar et al., 2015). (Siebesma and Cuijpers, 1995;Roode et al., 2012) studied the main parameters that affect warm cumulus clouds vertical velocity and defined the clouds' core as parts with positive buoyancy and positive updrafts. (Seigel, 2014) investigated shallow cumulus clouds using LES, and defined the cloud core as the positively buoyant part. He found that adding aerosols enhances turbulent mixing in the margins, which reduces the cloud's and cloud core's widths. (Wang et al., 2009) defined the core as the supersaturated part in the cloud, and showed that the negative buoyancy in the margins is due to evaporative cooling.

Here we explore the three different core definitions where the cloud core threshold is set to be a positive value (of buoyancy, vertical velocity, or supersaturation $(S-1)>0$) so that each definition partitions the cloud according to a fundamental physical process taking place during cloud growth. A cloud forms only if water droplets are activated and grow by diffusion. For condensation of vapor on water droplets to occur, a necessary condition is humidity supersaturation within a volume of air. The supersaturation core definition partitions the cloud to areas of condensation and evaporation. Since we consider convective clouds here, the only driver of supersaturation (see Eq. (2)) during cloud growth is upward vertical motion of air. Thus, the vertical velocity core partitions the cloud to areas where the saturation ratio increases (upward motion) or decreases (downward motion). Buoyancy is a measure for the vertical acceleration and its integral is the convective potential energy, or the fuel that drives cloud growth. Neglecting cases of large scale motion or air flow near obstacles, buoyancy is the main source for vertical momentum in the cloud. The buoyancy core partitions the cloud to areas of increase or decrease in the upward vertical motion.

The goals of this part of the work are to compare and understand the differences between the three basic definitions of cloud core (i.e. $W_{core}, RH_{core}, B_{core}$) throughout a convective cloud's lifetime, using both theoretical arguments and numerical simulations. The differences between the cores' evolution in time shed new light on the competition of processes within a cloud in time and space. Moreover, such an understanding can serve as a guideline to all studies that perform the partition to cloud core and margin, and assist in determining the relevance of a given partition. For simplicity, we focus here on warm convective clouds (only contain liquid water), avoiding the additional complexity and uncertainties associated with mixed phase and ice phase microphysics. In Part II of this work we demonstrate some of the insights gained by investigating differences between the different cores properties and their time evolution when changing the aerosol loading.

2. Methods

2.1. Single cloud model

For single cloud simulations we use the Tel-Aviv University axisymmetric, non-hydrostatic, warm convective single cloud model (TAU-CM). It includes a detailed (explicit) treatment of warm cloud microphysical processes solved by the multi-moment bin method (Feingold et al., 1988;Tzivion et al., 1989;Feingold et al., 1991;Tzivion et al., 1994). The warm microphysical processes included in the model are nucleation, diffusion (i.e. condensation and evaporation), collisional coalescence, breakup and sedimentation (for a more detailed description, see (Reisin et al., 1996)).

Convection was initiated using a thermal perturbation near the surface. A time step of 1 sec is chosen for dynamical computations, and 0.5 sec for the microphysical computations (e.g. condensation-evaporation). The total simulation time is 80 min. There are no radiation processes in the model. The domain size is 5x6 km, with an isotropic 50 m resolution. The model is initialized using a Hawaiian thermodynamic profile, based on the 91285 PHTO Hilo radiosonde at 00Z, 21 Aug, 2007. A typical oceanic size distribution of aerosols is chosen (Altaratz et al., 2008;Jaenicke, 1988), with a total concentration of 500 cm^{-3}. This concentration produced clouds that are non- to weakly- precipitating. In Part II additional aerosol concentrations are considered, including ones which produce heavy precipitation.

2.2. Cloud field model

Warm cumulus cloud fields are simulated using the System for Atmospheric Modeling (SAM) Model (version 6.10.3, for details see webpage: http://rossby.msrc.sunysb.edu/~marat/SAM.html) (Khairoutdinov and Randall, 2003)). SAM is a non-hydrostatic, anelastic model. Cyclic horizontal boundary conditions are used together with damping of gravity waves and maintaining temperature and moisture gradients at the model top. An explicit Spectral Bin Microphysics (SBM) scheme (Khain et al., 2004) is used. The scheme solves the same warm microphysical processes as in the TAU-CM single cloud model, and uses an identical aerosol size distribution and concentration (i.e. 500 cm^{-3}) for the droplet activation process.

We use the BOMEX case study as our benchmark for shallow warm cumulus fields. This case simulates a trade-wind cumulus (TCu) cloud field based on observations made near Barbados during June 1969 (Holland and Rasmusson, 1973). This case study has a well established initialization setup (sounding, surface fluxes, and surface roughness) and large scale forcing setup (Siebesma et al., 2003). It has been thoroughly tested in many previous studies (Heus et al., 2009;Jiang et al., 2006;Xue and Feingold, 2006;Grabowski and Jarecka, 2015). To check the robustness of the cloud field results, two additional case studies are simulated: (1) The same Hawaiian profile used to initiate the single cloud model, and (2) an Amazonian warm cumulus case based on the afternoon dry season mean profile for August 2001 obtained during the Large-scale Biosphere-Atmosphere (LBA) experiment data at Belterra, Brazil (Dias et al., 2012).

All three soundings (BOMEX, Hawaiian, and Amazonian) and surface properties used to initialize the model are detailed in (Heiblum et al., 2016b). The grid size is set to 100 m in the horizontal direction and 40 m in the vertical direction for all simulations. The domain size is 12.8 km x 12.8 km x 4 km for the BOMEX

Atmos. Chem. Phys. Discuss., https://doi.org/10.5194/acp-2018-780
Manuscript under review for journal Atmos. Chem. Phys.
Discussion started: 30 August 2018

Atmospheric Chemistry and Physics
Open Access
Discussions

simulation and extends to 5 km, 6 km in the vertical direction for the Hawaii and Amazon simulations, respectively. The time step for computation is 1 s for all simulations, with a total runtime of 8 hours. The initial temperature perturbations (randomly chosen within ± 0.1-1 ºC) are applied near the surface, during the first time step.

2.3. Physical and Geometrical Core definitions

A cloudy pixel is defined here as a grid-box with liquid water amount that exceeds 0.01 g kg^{-1}. The physical core of the cloud is defined using three different definitions: 1) RH_{core}: all grid boxes for which the relative humidity (RH) exceeds 100%, 2) B_{core}: buoyancy (see definition in Eq. (1)) above zero. The buoyancy is determined in each time step by comparing each cloudy pixel with the mean thermodynamic conditions for all non-cloudy pixels per vertical height, and 3) W_{core}: vertical velocity above zero. These definitions apply for both the single cloud and cloud field model simulations used here. Additional thresholds have also been checked for the updrafts or buoyancy definitions, yielding similar conclusions.

The centroid (i.e. mean location in each of the axes) is used here to represent the geometrical location of the total cloud (i.e. cloud geometrical core) and its specific physical cores. The distances between the total cloud and its cores' centroids, as presented here, are normalized to cloud size to reflect the relative distance between the two centroids, where 0 indicates coincident physical and geometrical cores and 1 indicates a physical core located at the cloud boundary. The single cloud simulations rely on an axisymmetric model and thus all centroids are horizontally located on the center axis while vertical deviations are permitted. For this model the distance is normalized by half the cloud's thickness. For the cloud field simulations both horizontal and vertical deviations are possible, therefore distances are normalized by the cloud's volume radius.

2.4. Center of gravity vs. Mass (CvM) phase space

Atmos. Chem. Phys. Discuss., https://doi.org/10.5194/acp-2018-780
Manuscript under review for journal Atmos. Chem. Phys.
Discussion started: 30 August 2018

Recent studies (Heiblum et al., 2016b, a) suggested the Center-of-Gravity vs. Mass (CvM) phase space as a useful approach to reduce the high dimensionally and to study results of large statistics of clouds during different stages of their lifetimes (such as seen in cloud fields). In this space, the Center-of-Gravity (COG) height and mass of each cloud in the field at each output time step (taken here to be 1 min) are collected and projected in the CvM phase space. This enables a compact view of all clouds in the simulation during all stages of their lifetimes. Although the scatter of clouds in the CvM is sensitive to the microphysical and thermodynamic settings of the cloud field, it was shown that the different subspaces in the CvM space correspond to different cloud processes and stages (Heiblum et al., 2016b, a). The lifetime of a cloud can be described by a trajectory on this phase space.

A schematic illustration of the CvM space in shown in Fig. 1. Most clouds are confined between the adiabat (curved dashed line) and the inversion layer base (horizontal dashed line). The adiabat curve corresponds to the theoretical evolution of a moist adiabat 1D cloud column in the CvM space. The large majority of clouds form within the growing branch (yellow shade) at the bottom left part of the space, adjacent to the adiabat. Clouds then follow the growing trajectory (grow in both COG and mass) to some maximal values. The growing branch deviates from the adiabat at large masses depending on the degree of sub-adiabaticity of the cloud field. After or during the growth stage of clouds, they may undergo the following processes: i) dissipate via a reverse trajectory along the growing one, ii) dissipate via a gradual dissipation trajectory (magenta shade), iii) shed off small mass cloud fragments (red shades), iv) in the case of precipitating clouds, they can shed off cloud fragments in the sub-cloudy layer (grey shade). The former two processes form continuous trajectories in the CvM space, while the latter two processes create disconnected subspaces.

2.5. Cloud tracking

To follow the evolution of individual clouds within a cloud field we use an automated 3D cloud tracking algorithm (see (Heiblum et al., 2016b) for details). It enables tracking of Continuous Cloud Entities (CCEs) from formation to dissipation, even if interactions between clouds (splitting or merging) occur during that lifetime. A CCE initiates as a new cloud forming in the field, and is tracked on the condition that it

Atmos. Chem. Phys. Discuss., https://doi.org/10.5194/acp-2018-780
Manuscript under review for journal Atmos. Chem. Phys.
Discussion started: 30 August 2018

retains the majority (>50%) of its mass during an interaction event if occurs. Thus, a CCE can terminate due to either cloud dissipation or cloud interactions.

3. Results - Single cloud simulation

The differences between the three types of core definitions are examined during the lifetime of a single cloud (Fig. 2), based on the Hawaiian profile. The cloud's total lifetime is 36 minutes (between t=7 and t=43 min of simulation). Each panel in Fig. 2 presents vertical cross-sections of the three cores (magenta - W_{core}, green - RH_{core}, and yellow - B_{core}) at four points in time (with 10-minute intervals). The cloud has an initial cloud base at 850m, and grows to a maximal top height of 2050 m. The condensation rates (red shades) increase toward the cloud center and the evaporation rates (blue shades) increase toward the cloud edges. Evaporation at the cloud top results in a large eddy below it that contributes to mixing and evaporation at the lateral boundaries of the cloud. Thus, a positive feedback is initiated which leads to cooling, negative buoyancy, and downdrafts. The dissipation of the cloud is accompanied with a rising cloud base and lowering of the cloud top.

During the growing stage (t=10, 20 min), when substantial condensation still occurs within the cloud, all of the cores seem to be self-contained within one another, with B_{core} being the smallest and W_{core} being the largest. During the final dissipation stages, when the cloud shows only evaporation (t=40), W_{core} and RH_{core} disappear while there is still a small B_{core} near the cloud top. Further analysis shows that the entire dissipating cloud is colder and more humid than the environment but downdrafts from the cloud top (see arrows in Fig. 2) promote adiabatic heating, and by that increase the buoyancy in dissipating cloudy pixels, sometimes reaching positive values. These buoyant pockets will be discussed further in Part II. The results indicate that the three types of physical cores of the cloud are not located around the cloud’s geometrical core along the whole cloud lifetime. During cloud growth the three types of cores surround the cloud's center, while during late dissipation the B_{core} is at offset from the cloud center.

For a more complete view of the evolution of the three core types in the single cloud case, time series of core fractions are shown in Fig. 3. Panels a and b show the core mass (core mass / total mass) and volume (core volume / total volume) fractions out of the cloud's totals. The results are similar for both measures expect for the fact that core mass fractions are larger than core volume fractions. This is due to significantly higher LWC per pixel in the cores compared to the margins, which skews the core mass fraction to higher values. Core mass fractions during the main cloud growing stage (between t=7 and t=27 min simulation time) are around 0.7 - 0.85 and core volume fractions are around 0.5 - 0.7. The time series show that as opposed to the W_{core} and RH_{core} fractions which decrease monotonically with time, B_{core} shows a slight increase during stages of cloud growth. In addition, for most of the cloud's lifetime the B_{core} fractions are the smallest and the W_{core} fractions are the largest, except for the final stage of the clouds dissipation where downdrafts from the cloud top creates pockets of positive buoyancy. These pockets are located at the cloud's peripheral regions rather than near the cloud's geometrical center as is typically expected for the cloud's core. In the cloud's center (the geometrical core) the B_{core} is the first one to terminate (at t=32 min) compared to both $W_{core}$and RH_{core} that decay together (at 36 min).

For describing the locations of the physical cores, we examine the distances between the cloud’s centroid and the cores’ centroids. The evolution of these distances is shown in Fig. 3c. At cloud initiation (t=7 min), when the cloud is very small, all cores’ centroids coincide with the total cloud centroid location. The B_{core} (and RH_{core} to a much lesser degree) centroid then deviates from the cloud centroid to a normalized distance of 0.27 (t=8 min). As cloud growth proceeds, B_{core} grows and its centroid coincides with the cloud’s centroid. All cores' centroids are located near the cloud centroid during the majority of the growing and mature stages of the cloud, showing normalized distances <0.1. During dissipation (t>27 min), the cores' centroid locations start to distance away from the cloud’s geometrical core followed by a reduction in distances due to the rapid loss of cloud volume. As mentioned above, it is shown that the regeneration of positive buoyancy at the end of cloud dissipation (t=40 min) takes place at the cloud edges, with normalized distance >0.5.

Finally, in Fig. 3d the fraction of pixels of each core contained within another core is shown. It can be seen that for the majority of cloud lifetime (up to t=33 min) B_{core} is subset (pixel fraction of 1) of RH_{core}, and the latter is a subset of W_{core}. As expected,

Atmos. Chem. Phys. Discuss., https://doi.org/10.5194/acp-2018-780
Manuscript under review for journal Atmos. Chem. Phys.
Discussion started: 30 August 2018

the other three permutations of pixel fractions (e.g. W_{core} in B_{core}) show much lower values. The cloudy regions that are not included within B_{core} but are included within the two other cores are exclusively at the cloud's boundaries (see Fig. 2). The same pattern is seen for cloudy regions that are included within W_{core} but not in RH_{core}. During the dissipation stage of the cloud its self-containing property (i.e. $B_{core} \subseteq RH_{core} \subseteq W_{core}$) breaks down. Similar temporal evolutions as shown here are seen for the other simulated clouds (with various aerosol concentrations) in part II of this work. A theoretical explanation for the different sizes of different core types and their subset properties is suggested in the next section.

4. Theoretical considerations explaining the single cloud simulation results

Here we propose simple physical considerations that predict the simulated difference in cloud partition to core and margin using different definitions. It should first be noted that by definition, water loading has a negative effect on buoyancy (see Eq. (1)) and constitutes a constant negative feedback during cloud convective growth. Nevertheless, the sign of buoyancy is dependent on cloud and environmental factors and cannot be generalized. We start with the idealized case of an adiabatic cloud and then add another layer of complexity and consider the effects of mixing of cloudy and non-cloudy air.

4.1. Adiabatic model

For the case of an adiabatic cloud column, the excess vapor above saturation is instantaneously converted to liquid (saturation adjustment). Thus, the adiabatic cloud is saturated (S=1) throughout its vertical profile, and only W_{core} and B_{core} differences can be considered. It is assumed that the adiabatic convective cloud is initiated by positive buoyancy initiating from the sub-cloudy layer. Neglecting the pressure gradient force, the vertical velocity at each height can be approximated by the convective available potential energy (CAPE) of the vertical column up to that height (Williams and Stanfill, 2002;Yano et al., 2005;Rennó and Ingersoll, 1996):

$$0.5w^2(h) = \int_{h_0}^{h} B(z)\,dz = CAPE(h) \quad (3).$$

Here we define CAPE to be the vertical integral of buoyancy from the lowest level of positive buoyancy (h_0, initiation of vertical velocity) to an arbitrary top height (h). As long as the cloud is growing it should have positive CAPE and will experience positive w throughout the column even if the local buoyancy at specific height is negative. Eventually the cloud must decelerate due to negative buoyancy and reach a top height, where CAPE = 0 and $w = 0$. Hence, for the adiabatic case, B_{core} is always a proper subset of W_{core} ($B_{core} \subset W_{core}$).

4.2. Cloud parcel entrainment model

In reality, clouds are not isolated and mixing with the environment must be taken into account. To test the effects of mixing on the cores, we first consider mixing between an adiabatic cloudy parcel and a non-cloudy environmental parcel. The details of these theoretical calculations are shown in Appendix A. The initial cloudy parcel is assumed to be saturated (part of RH_{core}), have positive vertical velocity (part of W_{core}), and experience either positive or negative buoyancy (part of $B_{core}\ or\ B_{margin}$), as is seen for the adiabatic column case. Additionally, mixing is assumed to be isobaric, and in a steady environment where the average temperature of the environment per a given height does not change. The resultant mixed parcel will have lower humidity content and lower LWC as compared to the initial cloudy parcel, and a new temperature. In nearly all cases (beside in an extremely humid environment) the mixed parcel will be sub-saturated and evaporation of LWC will occur. Evaporation ceases when equilibrium is reached due to air saturation (S=1) or due to complete evaporation of the droplets (which means S<1, and the mixed parcel is no longer cloudy since it has no liquid water content).

In addition to mixing between cloudy (core or margin) and non-cloudy parcels, mixing between core and margin parcels (within the cloud) also occurs. This mixing process can be considered as “entrainment-like” with respect to the cloud core. Considering the changes in the W_{core} and RH_{core}, there is no fundamental difference in the treatment of mixing of cloudy and non-cloudy parcels, or mixing between core and margin (because the margins and the environment are typically sub-saturated and experience negative vertical velocity). However, for the changes in the B_{core} after

Atmos. Chem. Phys. Discuss., https://doi.org/10.5194/acp-2018-780
Manuscript under review for journal Atmos. Chem. Phys.
Discussion started: 30 August 2018

mixing, there exists a fundamental difference between mixing *with* the reference temperature/humidity state (in the case of mixing with the environment) and mixing *given* a reference temperature/humidity state (in mixing between B_{core} and B_{margin}). Thus, it is interesting to check the effects of mixing between B_{core} and B_{margin} parcels on the total extent of the B_{core} with respect to the other two core types. The details of this second case are shown in Appendix B.

4.2.1. Effects of non-cloudy entrainment on buoyancy

When mixed with non-cloudy air, the change in buoyancy of the initial cloudy parcel (which is a part of $W_{core}$and $RH_{core}$and either B_{core} or B_{margin}) happens due to both mixing and evaporation processes. The theoretical calculations show that for all relevant temperatures (~0^{o}C to 30^{o}C, representing warm Cu), the change in the parcel's buoyancy due to evaporation alone will always be negative (see appendix A). It is because the negative effect of the temperature decrease overweighs the positive effects of the humidity increase and water loading decrease. Nevertheless, the total change in the buoyancy (due to both mixing and evaporation) depends on the initial temperature, relative humidity, and liquid water content of the cloudy and non-cloudy parcels.

In Fig. A1 a wide range of non-cloudy environmental parcels, each with their own thermodynamic conditions, are mixed with a saturated cloud parcel with either positive or negative buoyancy. The main conclusions regarding the effects of such mixing on the buoyancy are as follows:

i. To a first order, the initial buoyancy values are temperature dependent, where a cloudy parcel that is warmer (colder) by more than ~ 0.2^{o}C than the environment will be positively (negatively) buoyant for common values of cloudy layer environment relative humidity (RH>80%).

ii. Parcels that are initially part of B_{core} may only lower their buoyancy due to entrainment, either to positive or negative values depending on the environmental conditions.

Atmos. Chem. Phys. Discuss., https://doi.org/10.5194/acp-2018-780
Manuscript under review for journal Atmos. Chem. Phys.
Discussion started: 30 August 2018

iii. The lower the environmental RH, the larger the probability for parcel transition from B_{core} to B_{margin} after entrainment.

iv. Parcels that are initially part of B_{margin} can either increase or decrease their buoyancy value, but never become positively buoyant. The former case (buoyancy decrease) is expected be more prevalent since it occurs for the smaller range of temperature differences with the environment.

In summary, entrainment is expected to always have a net negative effect on B_{core} extent and B_{margin} values, while evaporation feedbacks serve to maintain RH_{core} in the cloud. Thus, we can predict that B_{core} should be a subset of RH_{core} (i.e. $B_{core} \subseteq RH_{core}$).

4.2.2. Effects of core and margin mixing on buoyancy

Here we consider the case of mixing between the B_{core} and $B_{margin,}$ meaning positively buoyant and negatively buoyant cloud parcels. For simplicity, we assume both parcels are saturated (S=1, both included in the RH_{core}). As seen above, such conditions exist in both the adiabatic case and in the case where an adiabatic cloud has undergone some entrainment with the environment. The buoyancy differences between the saturated parcels are mainly due to temperature differences, but also due to the increasing saturation vapor pressure with increasing temperature (see Appendix B for details).

In Fig. B1 is it shown that the resultant mixed parcel's buoyancy can be either positive or negative, depending on the magnitude of temperature difference of each parcel (core or margin) from that of the environment. However, in all cases the mixed parcel is supersaturated. This result can be generalized: given two parcels with equal RH but different temperature, the RH of the mixed parcel is always equal or higher than the initial value. Hence, B_{core} can either increase or decrease in extent, while the RH_{core} can only increase due to mixing between saturated B_{core} and B_{margin} parcels. This again strengthens the assumption that B_{core} should be a subset of RH_{core}.

We note that an alternative option for mixing between the core and margin parcels that exist here, where either or both of the parcels are subsaturated so that the mixed parcel is subsaturated as well. In this case evaporation will also occur. As seen in Appendix A, this should further reduce the buoyancy value of the mixed parcel (while increasing the RH).

4.2.3. Effects of entrainment on vertical velocity

We divide the entrainment effects on the W_{core} to two: i) a direct effect which includes conservation of momentum of vertical velocity between the core and margin/non-cloudy parcels, and ii) an indirect effect of vertical velocity changes due to buoyancy changes caused by the entrainment. The direct effect can be considered to occur instantaneously. Assuming homogeneous mixing of both parcels and a mixing fraction of 0.5, the direct effect can be simplified to conservation of momentum before and after mixing. Since both parcels are approximately of equal mass (in isobaric mixing), the mixed parcel's vertical velocity will be the average of the initial velocities. If the absolute value of the updraft in the W_{core} parcel is larger than that of the downdraft in the margin/non-cloudy parcel, the resultant mixed parcel will remain part of W_{core}. This is usually the case during the growing stages in clouds, where it can be assumed that the surrounding air around W_{core} is at rest or with downdrafts weaker than the updrafts within the W_{core}.

As opposed to the direct effect, the indirect effect is time dependent. The calculations in Appendix A indicates negative buoyancy values reaching -0.1 m/s^2 due to entrainment. However, measurements from within clouds show that the temperature deficiency of cloudy parcels with respect to the environment is generally restricted to less than 1^oC for cumulus clouds (Sinkevich and Lawson, 2005;Burnet and Brenguier, 2010;Wei et al., 1998;Malkus, 1958), and thus the negative buoyancy should be no more larger than -0.05 m/s^2. This value is closer to current and previous simulations and also observations that show negative buoyancy values within clouds to be confined between -0.001 and -0.01 m/s^2 (Roode et al., 2012;Ackerman, 1956). Given an initial vertical velocity of ~ 1 m/s, the deceleration due to buoyancy (and reversal to negative vertical velocity) should occur within a typical time range of 1 - 10 minutes. These timescales are much longer than the typical timescales of entrainment (mixing and evaporation that eliminate the B_{core}) which range between 1 – 10 s (Lehmann et al., 2009). Therefore, even if entrainment acts to reduce vertical velocity, it does so with substantial delay compared to the reduction of buoyancy, and B_{core} should be a subset of W_{core} (i.e. $B_{core} \subseteq W_{core}$) during the growing and mature stages of a cloud's lifetime.

4.3. The relation between supersaturation and vertical velocity cores

Here we revisit Eq. (2), and review the possible relations of W_{core} and RH_{core} in a warm convective cloud. A rising parcel initially has LWC=0 with its only source of supersaturation being the updraft w, and thus initially the RH_{core} should always be a proper subset of W_{core}. In general, since the sink term $\frac{dLWC}{dt}$ becomes a source only when S<1 (the condition for evaporation), the only way for a convective cloud to produce supersaturation (i.e. S>1) is by updrafts during all stages of its lifetime. Once supersaturation is achieved, the sink term becomes positive $\frac{dLWC}{dt} > 0$ and balances the updraft source term, so that supersaturation either increases or decreases. At any stage, if downdrafts replace the updrafts within a supersaturated parcel, the consequent change in supersaturation becomes strictly negative (i.e. $\frac{dS}{dt} < 0$). This negative feedback limits the possibility to find supersaturated cloudy parcels with downdrafts. Hence, we can expect the RH_{core} to be smaller than W_{core}, even though not necessarily a proper subset.

5. Results - Cloud field simulations

5.1. Partition to different core types

To test the robustness of the observed behaviors seen for a single cloud (and explained in the theoretical part), it is necessary to check whether they also apply to large statistics of clouds in a cloud field. The BOMEX simulation is taken for the analyses here. We discard the first 3 hours of cloud field data, during which the field spins-up and its mean properties are unstable. In Fig. 4 the volume and mass fractions of the three core types are compared for all clouds (at all output times – every 1 min) in the CvM space. As seen in Fig. 1, the location of specific clouds in the CvM space indicates their stage in evolution. Most clouds are confined to the region between the adiabat and the inversion layer base except for small precipitating (lower left region) and dissipating clouds (upper left region). The color shades of the clouds indicate whether a cloud is mostly core (red), mostly margin (blue), or equally divided to core and margin (white).

As seen for the single cloud, the core mass fractions tend to be larger than core volume fractions, for all core types. This is due to the fact that LWC values in the cloud core regions are higher than in margin regions, so that a cloud might be core dominated in terms of mass while being margin dominated in terms of volume. Focusing on the differences between core types, the color patterns in the CvM space imply that B_{core} definition yields the lowest core fractions (for both mass and volume), followed by RH_{core} with higher values and W_{core} with the highest values. The absence of the B_{core} is especially noticeable for small clouds in their initial growth stages after formation (COG ~ 550 m and LWP < 1 g m^{-2}). Those same clouds show the highest core fractions for the other two core definitions. This large difference can be explained by the existence of the transition layer (Garstang and Betts, 1974;Grant and Lock, 2004;Malkus, 1958;Neggers et al., 2007;de Roode and Bretherton, 2003) near the lifting condensation level (LCL) in warm convective cloud fields which is the approximated height of a convective cloud base (Meerkötter and Bugliaro, 2009;Craven et al., 2002). Within this layer parcels rising from the sub-cloudy layer are generally colder than parcels subsiding from the cloudy layer. Thus, this transition layer clearly marks the lower edge of the buoyancy core as most convective clouds are initially negatively buoyant.

Generally, the growing cloud branch (i.e. the CvM region closest to the adiabat) shows the highest core fractions. The RH_{core} and W_{core} fractions decrease with cloud growth (increase in mass and COG height) while the B_{core} initially increases, shows the highest fraction values around the middle region of the growing branch and then decreases for the largest clouds. The transition from the growing branch to the dissipation branch is manifested by a transition from core dominated to margin dominated clouds (i.e. transition from red to blue shades). Mixed within the margin dominated dissipating cloud branch, a scatter of W_{core} dominated small clouds can be

Atmos. Chem. Phys. Discuss., https://doi.org/10.5194/acp-2018-780
Manuscript under review for journal Atmos. Chem. Phys.
Discussion started: 30 August 2018

seen as well. These represent cloud fragments which shed off large clouds during their growing stages with positive vertical velocity. They are sometimes RH_{core} dominated as well but are strictly negatively buoyant. The few precipitating cloud fragments seen for this simulation (cloud scatter located below the adiabat) tend to be margin dominated, especially for the RH_{core}.

5.2. Self-contained properties of cores

From Fig. 4 it is clear that W_{core} tends to be the largest and B_{core} tends to be the smallest. To what degree however, are the cores self-contained within one another as was seen for the single cloud simulation? It is also interesting to check whether the different physical cores are centered near the cloud's geometrical core. In Fig. 5 the pixel fraction of each core type within another core type is shown for all clouds in the CvM space. A pixel fraction of 1 (bright colors) indicates that the pixels of the specific core in question (labeled in each panel title) completely overlap with the pixels of the other core (also labeled in the panel title) and a pixel fraction of 0 (dark colors) indicates zero overlap between the two cores in the cloud. It is seen that B_{core} tends to be a subset of both other cores, with pixel fractions around 0.75-1 for most of the growing branch area and large mass dissipating clouds which still have some positive buoyancy. The pixel fractions are higher for B_{core} inside W_{core} compared with B_{core} inside RH_{core}, but both show decrease with increase in growing branch cloud mass, meaning that chance for perfect self-containing of the cores decreases in large clouds.

The CvM space of RH_{core} inside W_{core} shows an even stronger relation between these two core types. For almost all growing branch clouds, the RH_{core} is a subset of W_{core} (i.e. $RH_{core} \subseteq W_{core}$). The pixel fractions decrease gradually with loss of cloud mass in the dissipation branch. The other three permutations of pixel fractions (W_{core} inside B_{core}, W_{core} inside RH_{core}, and RH_{core} inside B_{core}) give an indication of cores sizes and of which cloud types show no overlap between different cores. As stated above, growing (dissipation) clouds show higher (lower) overlap between the different core types. The W_{core} is almost twice as large as the B_{core} and 30%-40% larger than the RH_{core} along most of the growing branch. In conclusion, we see a strong tendency for the self-containing property of cores ($B_{core} \subseteq RH_{core} \subseteq W_{core}$) during the growth stages of clouds. This property ceases for dissipating and precipitating clouds, especially for the smaller clouds which show less overlap between core types.

In Fig. 6 the distances between the total cloud centroid and each specific physical core centroid locations are evaluated. Along the growing branch the cloud centroid and physical cores' centroids tend to be of close proximity, while during cloud dissipation the cores' centroids tend to increase in distance from the cloud's center. This type of evolution is most prominent for the W_{core}, which shows a clear gradient of transition from small (dark colors) to large (bright colors) distances. The B_{core} shows a more complex transition, from intermediate distance values (~0.5) at cloud formation, to near zeros values along the mature part of the growing branch, back to large values in the dissipation branch. Along the growing branch RH_{core} shows distances comparable to the W_{core} (except for large distances at cloud formation). However, compared to the other two core types, RH_{core} shows the smallest distances to the geometrical core during cloud dissipation. This is manifested by a relative absence of bright colors for dissipating clouds in Fig. 6.

The prevalence of cloud edge B_{core} pixels during dissipation can be explained by adiabatic heating due to weak downdrafts (see Sect. 4.2, Part II) which are expected at the cloud periphery. The fact that there is little overlap between B_{core} and both W_{core} and RH_{core} pixels in dissipating clouds (see Fig. 5) serves to verify this assumption. The relative absence of isolated RH_{core} pixels at the cloud edges can be explained by the fact the pixels closest to the cloud's edge are most susceptible to mixing with non-cloudy air and evaporation, yielding subsaturation conditions. The innermost pixels are "protected" from such mixing and thus we can expect most RH_{core} pixels to be located near the geometrical core.

The W_{core} case is less intuitive. During cloud dissipation complex patterns of updrafts and downdrafts within the cloud can create scenarios where the W_{core} centroid is located anywhere in the cloud. However, the results show that most small dissipating clouds tend to have their W_{core} pixels concentrated at the cloud edges. Comparing Fig. 6 with Figs. 4 and 5, we can see that these pixels comprise only a tiny fraction of the already small clouds and do not overlap with RH_{core} and B_{core} pixels and thus are not related to significant convection processes. Further analysis shows that the maximum updrafts in these clouds rarely exceed 0.5 m/s (i.e. 90% of clouds with normalized distance > 0.9 have a maximum updraft of less than 0.5 m/s), and can thus be considered with near neutral vertical velocity.

5.3. Consistency of the cloud partition to core types

The results for cloud fields are summarized in Fig. 7 that presents the evolution of core fractions of continuous cloud entities (CCEs, see Sect. 2.5 for details) from formation to dissipation. Only CCEs that undergo a complete life cycle are averaged here. These CCEs fulfill the following four conditions: i) form near the LCL, ii) live for at least 10 minutes, ii) reach maximum cloud mean LWP values above 10 g m^{-2}, and iv) terminate with mass value below 10 g m^{-2}. As a test of generality, we performed this analysis for Hawaiian and Amazonian warm cumulus cloud field simulations in addition to the BOMEX one. For each simulation, tens to hundreds of CCEs are collected (see panel titles) and their core fractions are averaged according to their normalized lifetimes (τ). Consistent results are seen for all three simulations. Clouds initiate with a W_{core} fraction of ~ 1, RH_{core} fraction of ~ 0.8, and B_{core} fraction of ~ 0.1. The former two core types' volume fraction decreases monotonically with lifetime, while the latter core type's volume fraction increases up to 0.3 at τ ~ 0.25, and then monotonically decreases for increasing τ. The fact that cloud's end their life cycle with non-zero volume fractions may indicate that some of the CCE terminate not because of full dissipation but rather because of significant splitting or merging events.

Normalized distances between core centroid and total cloud centroid (Fig. 7, middle column) tend to monotonically increase for RH_{core} and W_{core} with CCE lifetime for all simulations. The gradient of increase is larger at the later stages of CCE lifetime. Initially the W_{core} is closer to the geometrical core but at later stages of CCE lifetime (typically τ > 0.5) this switches and RH_{core} remains the closest. As seen above, for the first (second) half of CCE lifetime, the distance between B_{core} centroid and cloud centroid decreases (increases), starting at normalized distances above 0.4 for all simulations. The physical cores stay in proximity to the geometrical core for the majority of their lifetimes for the three cases. Taking the value 0.5 as a threshold for

Atmos. Chem. Phys. Discuss., https://doi.org/10.5194/acp-2018-780
Manuscript under review for journal Atmos. Chem. Phys.
Discussion started: 30 August 2018

transition from centered physical cores to periphery physical cores, Bomex, Hawaii, and Amazon simulation CCEs' W_{core} cross this threshold at τ = 0.94, 0.9, and 0.86, respectively. Thus, the assumption that a cloud's core (by any definition) is also indicative of the cloud's centroid is true for the majority of a typical cloud's lifetime.

The analysis of self-containing core properties (Fig. 7, right column) shows that the assumption $B_{core} \subseteq RH_{core} \subseteq W_{core}$ is true for the initial formation stages of a cloud. Although the corresponding pixel fractions decrease slightly during the lifetime of the CCE, they remain above 0.9 (e.g. B_{core} is 90% contained within RH_{core}). A sharp decrease in pixel fractions is seen for τ > 0.8, as the overlaps between the different cores is reduced during dissipation stages of the cloud. For all simulations, the highest pixel fraction values are seen for the B_{core} inside W_{core} pair, followed by RH_{core} insideW_{core} pair, and B_{core} inside RH_{core} pair showing slightly lower values. In addition, it can be seen that the variance of average pixel fraction (per τ) increases with increase in τ. This is due to the fact the all CCEs initiate with almost identical characteristics but may terminate in very different ways. In part II of this work we show that this variance is highly influenced from precipitation which contributes to more significant interactions between clouds (Heiblum et al., 2016a). Indeed, the Amazon simulation shows the largest pixel fraction variance and produces the most precipitation out of the three simulations.

6. Summary

In this paper we study the partition of warm convective clouds to core and margin according to three different definitions: i) positive vertical velocity (W_{core}), ii) relative humidity supersaturation (RH_{core}), and iii) positive buoyancy (B_{core}), with emphasis on the differences between those definitions. Using theoretical consideration of both an adiabatic cloud and a simple two parcel mixing model (see appendix A and B), we support our simulated results as we show that the B_{core} must be the smallest of the three. This is due to the fact that entrainment into the core (i.e. mixing with non-cloudy environment or mixing with the margin regions of the cloud) acts instantaneously to reduce cloud buoyancy values, for a wide range of thermodynamic conditions. In cases the mixed parcel is subsaturated, evaporation occurs and always has a negative effect on buoyancy. The same process has an opposing effect on the relative humidity of the mixed parcel and acts to reach saturation. Entrainment (or mixing) also acts to decrease vertical velocity, but at slower manner compared to the time scales of changes in the buoyancy and relative humidity. In addition, the supersaturation equation (Eq. (2)) predicts that it is unlikely to attain supersaturation in a cloudy volume with negative vertical velocity. Hence, W_{core} is expected to be the largest of the three cores.

Using numerical simulations of both a single cloud and cloud fields of warm cumulus clouds, we show that during most stages of clouds' lifetime, W_{core} is indeed the largest of the three and B_{core} the smallest. In addition to the differences in their sizes, the three cores tend to be subsets of one another (and located around the cloud geometrical center), in the following order: $B_{core} \subseteq RH_{core} \subseteq W_{core}$. This property is most valid for a cloud at its initial stages and breaks down gradually during a cloud's lifetime. The small B_{core} fractions (out of the total cloud) are due to two main reasons: i) buoyancy is strongly affected by mixing and evaporation, as the buoyant core is the first to disappear during the dissipation stages of a cloud, and ii) warm cloud fields typically have a transition layer near the lifting condensation level (LCL), where ascending parcels are colder than descending parcels so the lower parts of the clouds are negatively buoyant. After cloud formation internal growth processes (i.e. condensation and latent heat release) increase the B_{core} until dissipation processes become dominant and the core decreases quickly. In contrast, clouds are initially dominated by the W_{core} and RH_{core} (fractions close to 1). The fractions of these cores then decrease monotonically with cloud lifetime.

During dissipation stages, the clouds are mostly margin dominated, such that most of the small mass dissipation cloud fragments are entirely coreless. However, several small mass dissipating cloud fragments which shed off large cloud entities (with large COG height) may be core dominated, especially using the RH_{core} definition. The same is observed for small precipitating cloud fragments which reside below the convective cloud base. We note that the results here are similar for both volume and mass core fractions out the cloud's totals, with the core mass fractions being larger due to a skewed distribution of cloud LWC which favors the core regions. Moreover, we show that these results are consistent for various levels of aerosol concentrations

Atmos. Chem. Phys. Discuss., https://doi.org/10.5194/acp-2018-780
Manuscript under review for journal Atmos. Chem. Phys.
Discussion started: 30 August 2018

(will be seen in Part II) and different thermodynamic profiles used to initialize the models.

With respect to cloud morphology, it is shown that during cloud growth, which comprises the majority of a warm cloud lifetime, the physical cores are centered near the cloud's geometrical core, as is intuitively expected from a cloud's core. An exception to this is the initial growth stages, where the B_{core} centroid can be located far from the cloud's centroid. During dissipation, the cores decouple from the geometrical core and often comprise just a few isolated pixels at the cloud's edges. The W_{core} and B_{core} pixels tend to be more peripheral than RH_{core} during dissipation (see Sect. 5.2). Downdraft induced adiabatic heating at the clouds' edge (see more in Part II) promote positive buoyancy while decreasing the chance for supersaturation. During dissipation the overlap between different core types also decreases rapidly, implying that minor local effects enable core existence rather than cloud convection. Thus, only during mature growth stages can all three cores types can be considered interchangeable. In Part II of this work we use the insights gained here to understand aerosol effects on warm convective clouds, as are reflected by a cloud's partition to its core and margin.

Acknowledgements

The research leading to these results was supported by the Ministry of Science & Technology, Israel (grant no. 3-14444).

Appendix A: Buoyancy changes due to mixing of cloudy and non-cloudy parcels

Here we present a simple model for entrainment mixing between a cloudy parcel (either part of B_{core} or B_{margin}) and a dry environmental parcel. Entrainment mixes the momentum, heat, and humidity of the two parcels. We consider the mixing of a unit mass of cloud parcel which is defined by two criteria:

$$S_1 \geq 1$$
$$B_1 > 0 \; or \; B_1 < 0$$

with a unit mass of dry environment parcel, defined by:

$$S_2 < 1$$

Atmos. Chem. Phys. Discuss., https://doi.org/10.5194/acp-2018-780
Manuscript under review for journal Atmos. Chem. Phys.
Discussion started: 30 August 2018

and explore the properties of the resulting mixed parcel.

Assume that T_1, T_2, T_3 are the initial temperatures of the cloudy, environmental, and resulting mixed parcel, respectively. q_{v1}, q_{v2}, q_{v3}, $\theta_1, \theta_2, \theta_3$, and $q_{l_1}, q_{l_2}, q_{l_3}$ are their respective vapor mixing ratios, potential temperatures, and liquid water contents (LWC).

The change in buoyancy due to mixing will be:

$$dB_{mix} = g * \left(\frac{\theta_3 - \theta_1}{\theta_2} + 0.61(q_{v3} - q_{v1}) - (q_{l_3} - q_{l_1})\right) \quad \text{(A1),}$$

with

$$T_3 = \mu_1 \cdot T_1 + \mu_2 \cdot \mathrm{T}_2 \quad \text{(A2),}$$

$$q_{v3} = \mu_1 \cdot q_{v1} + \mu_2 \cdot q_{\mathrm{v}2} \quad \text{(A3),}$$

$$q_{l_3} = \mu_1 \cdot q_{l_1} + \mu_2 \cdot q_{l_2} \quad \text{(A4),}$$

where μ_1 and μ_2 are the corresponding mixing fractions. We assume that the mixed parcel is at the same height as the cloudy and environmental parcels, and that the mean environmental temperature at that height stays the same after mixing. The potential temperature (θ) is calculated using its definition.

After the mixing process, the resultant mixed parcel may be subsaturated ($S_3 < 1$), and cloud droplets start to evaporate. The evaporation process increases the humidity of the parcel. ((Korolev et al., 2016), Eq. (A8)) calculated the amount of the required liquid water for evaporation, in order to reach S=1 again:

$$\delta q = \frac{C_p R_v T_2^2}{L^2} ln\left(\frac{1+\frac{e_s(T_3) R_a L^2}{P C_p R_v^2 T_3^2}}{1+S_3 \frac{e_s(T_3) R_a L^2}{P C_p R_v^2 T_3^2}}\right) \quad \text{(A5),}$$

Where C_p is a specific heat at constant pressure,$e_s(T_3)$ is the saturated vapor pressure for the mixed temperature, P is pressure, L is latent heat, R_v, R_a are individual gas constants for water vapor and dry air, respectively. If the mixed parcel contains sufficient LWC to evaporate δq amount of water, the mixed parcel will reach saturation. We note that Eq. (A5) holds for cases where $|T_1 - T_2| < 10^o C$, which is well within the range seen in our simulations of warm clouds.

Atmos. Chem. Phys. Discuss., https://doi.org/10.5194/acp-2018-780
Manuscript under review for journal Atmos. Chem. Phys.
Discussion started: 30 August 2018

Assuming the average environmental temperature stays the same after evaporation, the buoyancy after evaporation is calculated using the following formulas:

$$dB_{evap} = g \cdot \left(\frac{d\theta'_{evap}}{\theta_2} + 0.61 dq_{v_{evap}} + dq_{l_{evap}} \right) \quad \text{(A6)},$$

$$d\theta'_{evap} = dT_{evap} \quad \text{(A7)},$$

From the first law of thermodynamics:

$$C_p \cdot dT_{evap} = -L \cdot dq_{v_{evap}} \quad \text{(A8)}.$$

The water vapor is the amount of liquid water lost by evaporation:

$$dq_{v_{evap}} = -dq_{l_{evap}} = \delta q \quad \text{(A9)},$$

From the above we get:

$$dB_{evap} = g \cdot \delta q \left(1.61 - \frac{L}{C_p \theta_2} \right) \quad \text{(A10)}.$$

For a wide temperature range between $200 < \bar{\theta}_2 < 300[K]$, dB_{evap} is always negative. This result is not trivial because evaporation both decreases the T and increases the q_v which have opposite effects. The total change in buoyancy is taken as the sum of dB_{evap} and dB_{mix}.

Figure A1 presents a phase space of possible changes in cloudy pixel buoyancy due to mixing with outside air, for various thermodynamic conditions, and a mixing fraction of 0.5. The initial cloudy parcel is chosen to be saturated (S=1) and includes a LWC of 1 g kg^{-1}. The pressure is assumed to be 850 mb, and the temperature 15^oC. However, we note that the conclusions here apply to all atmospherically relevant values of pressure, temperature, supersaturation (values of RH>100%), and LWC in warm clouds. The X-axis in Fig. A1 spans a range of non-cloudy environment relative humidity values (60% < RH < 100%), and the Y-axis spans a temperature difference range between the cloud and the environment parcels ($-3° < dT < 3°$). The initial (B_i) and final (B_f, after entrainment) buoyancy values, and the differences between them can be either positive or negative. The regions of B_i>0 (B_i<0) in fact illustrate the effects of entrainment on B_{core} (B_{margin}) parcels.

Atmos. Chem. Phys. Discuss., https://doi.org/10.5194/acp-2018-780
Manuscript under review for journal Atmos. Chem. Phys.
Discussion started: 30 August 2018

Appendix B: **Buoyancy changes due to mixing of core and margin parcels**

Following the notations of appendix A, we now consider the mixing of two cloudy parcels, one part of B_{core} and one part of B_{margin}. For simplicity, we choose the case where both parcels are saturated and have the same LWC of 0.5 g kg^{-1}:

$$\begin{gathered} S_{core} = S_{margin} = S_{cloud} = 1 \\ q_{l_{core}} = q_{l_{margin}} = q_{l_{cloud}} = 0.5 \end{gathered} \qquad \text{(B1).}$$

The buoyancy of each cloudy parcel is determined in reference to the environmental temperature and humidity, $T_{env}, q_{v_{env}}$, so that:

$$B_{cloud} = g * \left(\frac{\theta_{cloud} - \theta_{env}}{\theta_{env}} + 0.61\left(q_{v_{cloud}} - q_{v_{env}}\right) - q_{l_{cloud}}\right) \qquad \text{(B2).}$$

As mentioned in the main text, we take a temperature range of $T_{env} - 3°c < T_{cloud} < T_{env} + 3°c$. Each cloudy parcel's temperature also dictates its saturation vapor pressure $e_s(T_{cloud})$ and therefore also its humidity content, $q_{v_{cloud}}$. Plugging these into Eq. (B2), one can associate each temperature/humidity pair with the B_{core} or B_{margin}:

$$\begin{gathered} T_{core} = T_{cloud}(B_{cloud} > 0),\ q_{v_{core}} = q_{v_{cloud}}(B_{cloud} > 0) \\ T_{margin} = T_{cloud}(B_{cloud} < 0), q_{v_{margin}} = q_{v_{cloud}}(B_{cloud} < 0) \end{gathered} \qquad \text{(B3).}$$

The core and margin parcels can then be mixed (see appendix A) yielding a mixed parcel temperature and humidity content, and thus a new relative humidity. The buoyancy of the mixed parcel is obtained by inserting these parameters in Eq. (B2).

In Fig. B1 the resultant buoyancy values and RH values after the mixing of B_{core} parcels with B_{margin} parcels are shown. As defined in Appendix A, temperature differences between the parcels and the environment are confined to ±3^{o}C. The reference environmental temperature, pressure, and RH are taken to be 15^{o}C, 850 mb, and 90%, respectively. We note the main differences between this section and Appendix A are the absence of evaporation and the fact that the core and margin thermodynamic variables are the ones that vary while the reference environmental ones are kept constant.

Atmos. Chem. Phys. Discuss., https://doi.org/10.5194/acp-2018-780
Manuscript under review for journal Atmos. Chem. Phys.
Discussion started: 30 August 2018

It can be seen that all negatively buoyant parcels are colder than the environment and nearly all positively buoyant parcels are warmer than the environment, except for a small fraction that are slightly colder but positively buoyant due to the increased humidity. The transition from $B_f>0$ to $B_f<0$ near the 1 to 1 line indicates that B_f is approximately linearly dependent on the temperature differences with respect to the environment. In other words, if $|T_{core} - T_{env}| > |T_{margin} - T_{env}|$, the mixed parcel is expected to be part of the B_{core} (i.e. $B_f>0$). The exponential increase in saturation vapor pressure with temperature is demonstrated by the results of the mixed parcel final RH, which all show supersaturation values. Additional sensitivity tests were performed for this analysis, showing only weak dependencies on environmental parameter values, while maintaining the main conclusions.

References

Ackerman, B.: BUOYANCY AND PRECIPITATION IN TROPICAL CUMULI, Journal of Meteorology, 13, 302-310, 10.1175/1520-0469(1956)013<0302:bapitc>2.0.co;2, 1956.

Altaratz, O., Koren, I., Reisin, T., Kostinski, A. B., Feingold, G., Levin, Z., and Yin, Y.: Aerosols' influence on the interplay between condensation, evaporation and rain in warm cumulus cloud, Atmos Chem Phys, 8, 15-24, 10.5194/acp-8-15-2008, 2008.

Burnet, F., and Brenguier, J.-L.: The onset of precipitation in warm cumulus clouds: An observational case-study, Quarterly Journal of the Royal Meteorological Society, 136, 374-381, 10.1002/qj.552, 2010.

Craven, J. P., Jewell, R. E., and Brooks, H. E.: Comparison between Observed Convective Cloud-Base Heights and Lifting Condensation Level for Two Different Lifted Parcels, Weather and Forecasting, 17, 885-890, 10.1175/1520-0434(2002)017<0885:CBOCCB>2.0.CO;2, 2002.

Dagan, G., Koren, I., and Altaratz, O.: Competition between core and periphery-based processes in warm convective clouds – from invigoration to suppression, Atmos. Chem. Phys., 15, 2749-2760, 10.5194/acp-15-2749-2015, 2015.

de Roode, S. R., and Bretherton, C. S.: Mass-flux budgets of shallow cumulus clouds, J Atmos Sci, 60, 137-151, 10.1175/1520-0469(2003)060<0137:MFBOSC>2.0.CO;2, 2003.

Atmos. Chem. Phys. Discuss., https://doi.org/10.5194/acp-2018-780
Manuscript under review for journal Atmos. Chem. Phys.
Discussion started: 30 August 2018

Feingold, G., Tzivion, S., and Leviv, Z.: Evolution of Raindrop Spectra. Part I: Solution to the Stochastic Collection/Breakup Equation Using the Method of Moments, J Atmos Sci, 45, 3387-3399, 10.1175/1520-0469(1988)045<3387:eorspi>2.0.co;2, 1988.

Feingold, G., Levin, Z., and Tzivion, S.: The Evolution of Raindrop Spectra. Part III: Downdraft Generation in an Axisymmetrical Rainshaft Model, J Atmos Sci, 48, 315-330, 10.1175/1520-0469(1991)048<0315:teorsp>2.0.co;2, 1991.

Garstang, M., and Betts, A. K.: A Review of the Tropical Boundary Layer and Cumulus Convection: Structure, Parameterization, and Modeling, Bulletin of the American Meteorological Society, 55, 1195-1205, 10.1175/1520-0477(1974)055<1195:AROTTB>2.0.CO;2, 1974.

Grabowski, W. W., and Jarecka, D.: Modeling Condensation in Shallow Nonprecipitating Convection, J Atmos Sci, 72, 4661-4679, 10.1175/JAS-D-15-0091.1, 2015.

Grant, A. L. M., and Lock, A. P.: The turbulent kinetic energy budget for shallow cumulus convection, Quarterly Journal of the Royal Meteorological Society, 130, 401-422, 10.1256/qj.03.50, 2004.

Heiblum, R. H., Altaratz, O., Koren, I., Feingold, G., Kostinski, A. B., Khain, A. P., Ovchinnikov, M., Fredj, E., Dagan, G., Pinto, L., Yaish, R., and Chen, Q.: Characterization of cumulus cloud fields using trajectories in the center of gravity versus water mass phase space: 2. Aerosol effects on warm convective clouds, Journal of Geophysical Research: Atmospheres, 121, 6356-6373, 10.1002/2015JD024193, 2016a.

Heiblum, R. H., Altaratz, O., Koren, I., Feingold, G., Kostinski, A. B., Khain, A. P., Ovchinnikov, M., Fredj, E., Dagan, G., Pinto, L., Yaish, R., and Chen, Q.: Characterization of cumulus cloud fields using trajectories in the center of gravity versus water mass phase space: 1. Cloud tracking and phase space description, Journal of Geophysical Research: Atmospheres, 121, 6336-6355, 10.1002/2015JD024186, 2016b.

Heus, T., Jonker, H. J. J., Van den Akker, H. E. A., Griffith, E. J., Koutek, M., and Post, F. H.: A statistical approach to the life cycle analysis of cumulus clouds selected in a virtual reality environment, Journal of Geophysical Research: Atmospheres, 114, D06208, 10.1029/2008JD010917, 2009.

Atmos. Chem. Phys. Discuss., https://doi.org/10.5194/acp-2018-780
Manuscript under review for journal Atmos. Chem. Phys.
Discussion started: 30 August 2018

Holland, J. Z., and Rasmusson, E. M.: Measurements of the atmospheric mass, energy, and momentum budgets over a 500-kilometer square of tropical ocean, Monthly Weather Review, 101, 44-55, 10.1175/1520-0493(1973)101<0044:MOTAME>2.3.CO;2, 1973.

IPCC: Clouds and Aerosols, in: *Climate Change 2013 - The Physical Science Basis*, Cambridge University Press, 571-658, 2013.

Jaenicke, R.: 9.3.1 Physical properties, in: Physical and Chemical Properties of the Air, edited by: Fischer, G., Springer Berlin Heidelberg, Berlin, Heidelberg, 405-420, 1988.

Jiang, H., Xue, H. W., Teller, A., Feingold, G., and Levin, Z.: Aerosol effects on the lifetime of shallow cumulus, Geophysical Research Letters, 33, 10.1029/2006gl026024, 2006.

Khain, A. P., Pokrovsky, A., Pinsky, M., Seifert, A., and Phillips, V.: Simulation of Effects of Atmospheric Aerosols on Deep Turbulent Convective Clouds Using a Spectral Microphysics Mixed-Phase Cumulus Cloud Model. Part I: Model Description and Possible Applications, J Atmos Sci, 61, 2963-2982, 10.1175/JAS-3350.1, 2004.

Khairoutdinov, M. F., and Randall, D. A.: Cloud Resolving Modeling of the ARM Summer 1997 IOP: Model Formulation, Results, Uncertainties, and Sensitivities, J Atmos Sci, 60, 607-625, 10.1175/1520-0469(2003)060<0607:CRMOTA>2.0.CO;2, 2003.

Khairoutdinov, M. F., Krueger, S. K., Moeng, C.-H., Bogenschutz, P. A., and Randall, D. A.: Large-Eddy Simulation of Maritime Deep Tropical Convection, J Adv Model Earth Sy, 1, n/a-n/a, 10.3894/JAMES.2009.1.15, 2009.

Korolev, A., Khain, A., Pinsky, M., and French, J.: Theoretical study of mixing in liquid clouds – Part 1: Classical concepts, Atmos. Chem. Phys., 16, 9235-9254, 10.5194/acp-16-9235-2016, 2016.

Kumar, V. V., Jakob, C., Protat, A., Williams, C. R., and May, P. T.: Mass-Flux Characteristics of Tropical Cumulus Clouds from Wind Profiler Observations at Darwin, Australia, J Atmos Sci, 72, 1837-1855, 10.1175/jas-d-14-0259.1, 2015.

Lebo, Z. J., and Seinfeld, J. H.: Theoretical basis for convective invigoration due to increased aerosol concentration, Atmos. Chem. Phys, 11, 5407-5429, 10.5194/acp-11-5407-2011, 2011.

Atmos. Chem. Phys. Discuss., https://doi.org/10.5194/acp-2018-780
Manuscript under review for journal Atmos. Chem. Phys.
Discussion started: 30 August 2018

Atmospheric Chemistry and Physics
Discussions
Open Access

Lehmann, K., Siebert, H., and Shaw, R. A.: Homogeneous and inhomogeneous mixing in cumulus clouds: Dependence on local turbulence structure, J Atmos Sci, 66, 3641-3659, 2009.

Malkus, J. S.: On the structure of the trade wind moist layer, 10.1575/1912/5443, 1958.

Meerkötter, R., and Bugliaro, L.: Diurnal evolution of cloud base heights in convective cloud fields from MSG/SEVIRI data, Atmos Chem Phys, 9, 1767-1778, 10.5194/acp-9-1767-2009 2009.

Morrison, H.: On the robustness of aerosol effects on an idealized supercell storm simulated with a cloud system-resolving model, Atmos. Chem. Phys., 12, 7689-7705, 10.5194/acp-12-7689-2012, 2012.

Neggers, R. A. J., Stevens, B., and Neelin, J. D.: Variance scaling in shallow-cumulus-topped mixed layers, Quarterly Journal of the Royal Meteorological Society, 133, 1629-1641, 10.1002/qj.105, 2007.

Pinsky, M., Mazin, I. P., Korolev, A., and Khain, A. P.: Supersaturation and Diffusional Droplet Growth in Liquid Clouds, J Atmos Sci, 70, 2778-2793, 10.1175/JAS-D-12-077.1, 2012.

Reisin, T., Levin, Z., and Tzivion, S.: Rain Production in Convective Clouds As Simulated in an Axisymmetric Model with Detailed Microphysics. Part I: Description of the Model, J Atmos Sci, 53, 497-519, 10.1175/1520-0469(1996)053<0497:RPICCA>2.0.CO;2, 1996.

Rennó, N. O., and Ingersoll, A. P.: Natural Convection as a Heat Engine: A Theory for CAPE, J Atmos Sci, 53, 572-585, 10.1175/1520-0469(1996)053<0572:ncaahe>2.0.co;2, 1996.

Roode, S. R. d., Siebesma, A. P., Jonker, H. J. J., and Voogd, Y. d.: Parameterization of the Vertical Velocity Equation for Shallow Cumulus Clouds, Monthly Weather Review, 140, 2424-2436, 10.1175/mwr-d-11-00277.1, 2012.

Seigel, R. B.: Shallow Cumulus Mixing and Subcloud-Layer Responses to Variations in Aerosol Loading, J Atmos Sci, 71, 2581-2603, 10.1175/JAS-D-13-0352.1, 2014.

Siebesma, A. P., and Cuijpers, J. W. M.: Evaluation of parametric assumptions for shallow cumulus convection, J Atmos Sci, 52, 650-666, 10.1175/1520-0469(1995)052<0650:EOPAFS>2.0.CO;2, 1995.

Siebesma, A. P., Bretherton, C. S., Brown, A., Chlond, A., Cuxart, J., Duynkerke, P. G., Jiang, H., Khairoutdinov, M. F., Lewellen, D., and Moeng, C. H.: A large eddy

Atmos. Chem. Phys. Discuss., https://doi.org/10.5194/acp-2018-780
Manuscript under review for journal Atmos. Chem. Phys.
Discussion started: 30 August 2018

Atmospheric Chemistry and Physics
Discussions

simulation intercomparison study of shallow cumulus convection, J Atmos Sci, 60, 1201-1219, 10.1175/1520-0469(2003)60<1201:ALESIS>2.0.CO;2, 2003.

Sinkevich, A. A., and Lawson, R. P.: A Survey of Temperature Measurements in Convective Clouds, Journal of Applied Meteorology, 44, 1133-1145, 10.1175/JAM2247.1, 2005.

Trenberth, K. E., Fasullo, J. T., and Kiehl, J.: Earth's global energy budget, Bull. Amer. Meteor. Soc, 90, 311-323, 10.1175/2008BAMS2634.1, 2009.

Tzivion, S., Feingold, G., and Levin, Z.: The Evolution of Raindrop Spectra. Part II: Collisional Collection/Breakup and Evaporation in a Rainshaft, J Atmos Sci, 46, 3312-3328, 10.1175/1520-0469(1989)046<3312:teorsp>2.0.co;2, 1989.

Tzivion, S., Reisin, T., and Levin, Z.: Numerical Simulation of Hygroscopic Seeding in a Convective Cloud, Journal of Applied Meteorology, 33, 252-267, 10.1175/1520-0450(1994)033<0252:nsohsi>2.0.co;2, 1994.

Wang, Y., Geerts, B., and French, J.: Dynamics of the Cumulus Cloud Margin: An Observational Study, J Atmos Sci, 66, 3660-3677, doi:10.1175/2009JAS3129.1, 2009.

Wei, D., Blyth, A. M., and Raymond, D. J.: Buoyancy of convective clouds in TOGA COARE, J Atmos Sci, 55, 3381-3391, 1998.

Williams, E., and Stanfill, S.: The physical origin of the land–ocean contrast in lightning activity, Comptes Rendus Physique, 3, 1277-1292, 10.1016/S1631-0705(02)01407-X, 2002.

Xue, H. W., and Feingold, G.: Large-eddy simulations of trade wind cumuli: Investigation of aerosol indirect effects, J Atmos Sci, 63, 1605-1622, 10.1175/jas3706.1, 2006.

Yano, J.-I., Chaboureau, J.-P., and Guichard, F.: A generalization of CAPE into potential-energy convertibility, Quarterly Journal of the Royal Meteorological Society, 131, 861-875, 10.1256/qj.03.188, 2005.

Figures

Atmos. Chem. Phys. Discuss., https://doi.org/10.5194/acp-2018-780
Manuscript under review for journal Atmos. Chem. Phys.
Discussion started: 30 August 2018

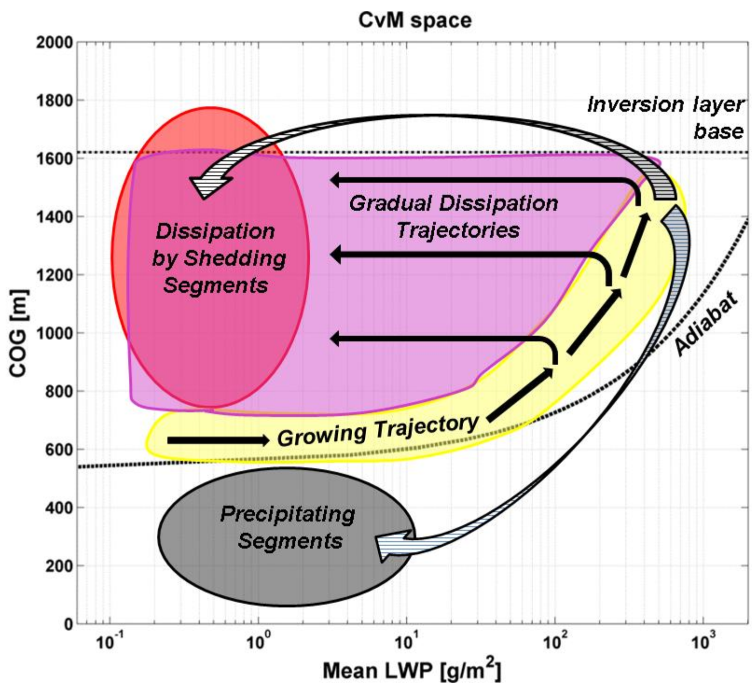

Figure 1. A schematic representation of a cloud field Center-of-gravity height (Y-Axis) vs. Mass (X-Axis) phase space (CvM in short). The majority of clouds are confined to the region between the adiabatic approximation (curved dashed line) and the inversion layer base height (horizontal dashed line). The yellow, magenta, red, and grey shaded regions represent cloud growth, gradual dissipation, cloud fragments which shed off large clouds, and cloud fragments which shed off precipitating clouds, respectively. The black arrows represent continuous trajectories of cloud growth and dissipation. The hatched arrows represent two possible discontinuous trajectories of cloud dissipation where clouds shed segments.

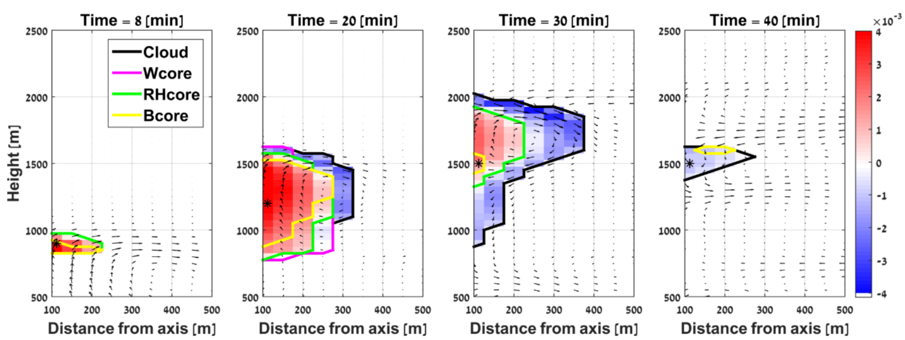

Atmos. Chem. Phys. Discuss., https://doi.org/10.5194/acp-2018-780
Manuscript under review for journal Atmos. Chem. Phys.
Discussion started: 30 August 2018

Atmospheric Chemistry and Physics
Discussions

Figure 2. Four vertical cross-sections (at t=10, 20, 30, 40 minutes) during the single cloud simulation. Y-axis represents height [m] and X-axis represents the distance from the axis [m]. The black, magenta, green and yellow lines represent the cloud, W_{core}, RH_{core} and B_{core}, respectively. The black arrows represent the wind, the background represents the condensation (red) and evaporation rate (blue) [g kg^{-1} s^{-1}], and the black asterisks indicate the vertical location of the cloud centroid. Note that in some cases the lines indicating core boundaries overlap (mainly seen for RH and W cores).

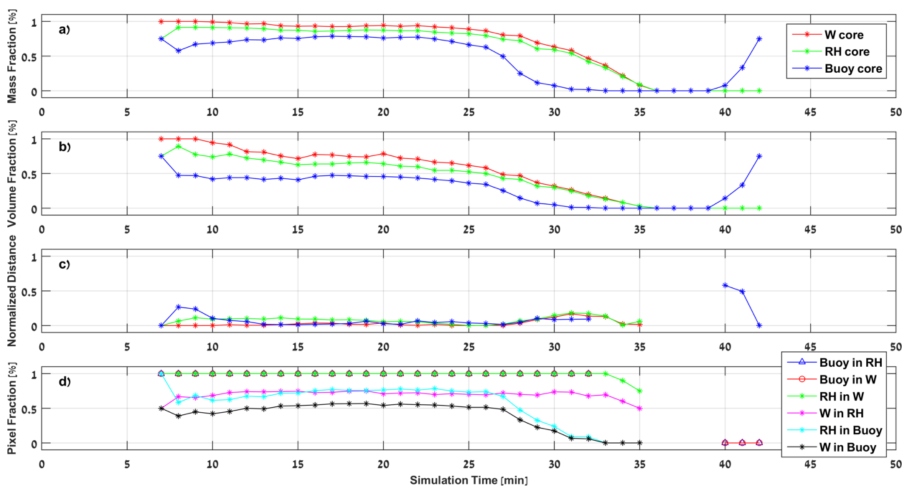

Figure 3. Temporal evolution of selected core properties, including: (a) The fraction of the cores' mass from the total cloud mass, (b) the fraction of the cores' volume from the total cloud volume, (c) the normalized distance between cloud centroid and core centroid, and (d) the fraction of cores' pixels contained within another core, including all six permutations. See panel legends for descriptions of line colors.

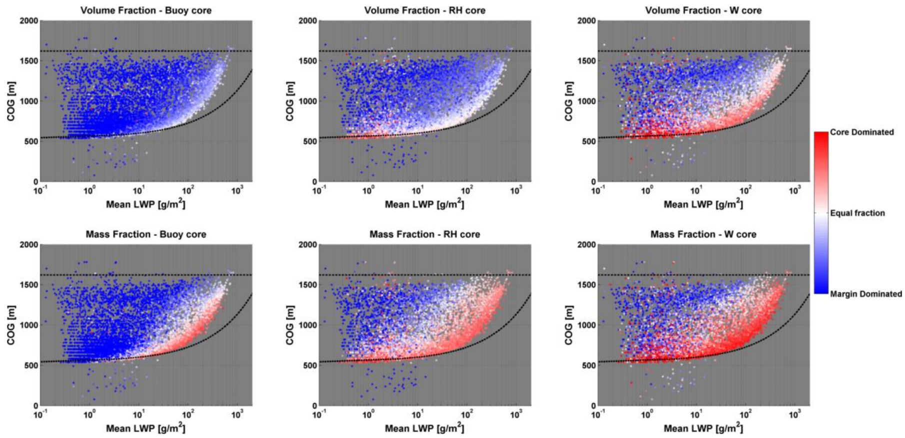

Figure 4. CvM phase space diagrams of B_{core} (left column), RH_{core} (middle column), and W_{core} (right column) fractions for all clouds between 3 h and 8 h in the BOMEX simulation. Both volume fractions (upper panels) and mass fractions (lower panels) are shown. The red (blue) colors indicate a core fraction above (below) 0.5. For a general description of CvM space characteristics the reader is referred to Sect. 2.4.

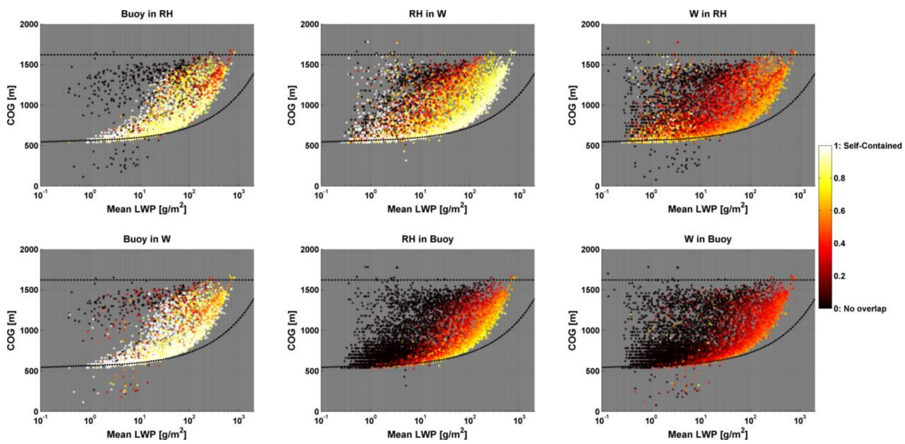

Figure 5. CvM phase space diagrams of pixel fractions of each of the three cores within another core, including six different permutations (as indicated in the panel titles). Bright colors indicate high pixel fractions (large overlap between two core types) while dark colors indicate low pixel fraction (little overlap between two core types). The differences in the scatter density and location for different panels are due to the fact that only clouds which contain a core fraction above zero (for the core in

question) are considered. For example, for the Buoy in RH panel (upper left), only cloud that contain some pixels with positive buoyancy are considered.

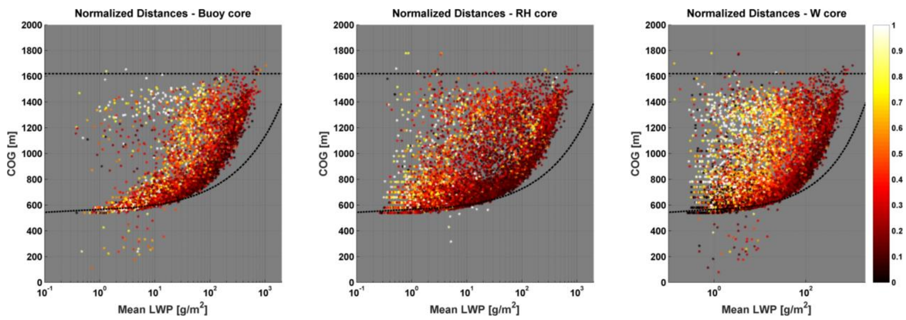

Figure 6. CvM phase space diagrams of distances between core centroid location and cloud centroid location, for the three different physical core types. The distances are normalized by the cloud volume radius (approximately the largest distance possible). Bright (dark) colors indicates large (small) distances. As seen in Fig. 5, only clouds which contain a core fraction above zero (for the core in question) are considered.

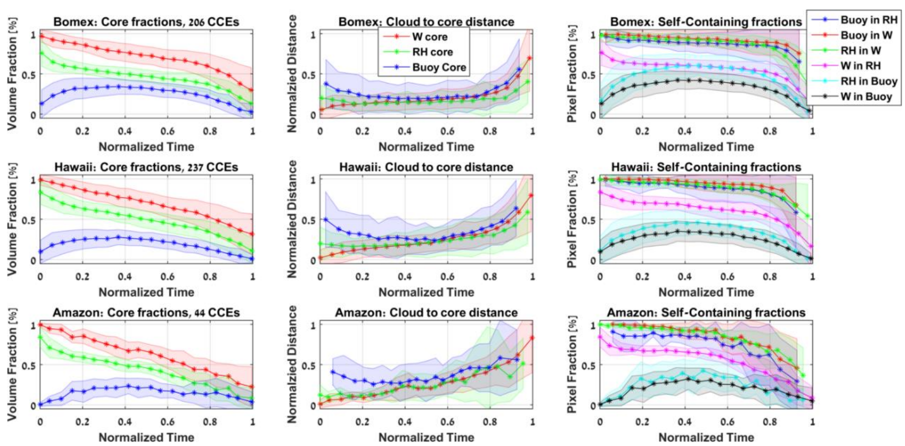

Figure 7. Normalized time (τ) series of CCE averaged core fractions for the BOMEX (upper row), Hawaii (middle row), and Amazon (bottom row) simulations. Both core volume fractions (left column), normalized distances between cloud and core centroid

Atmos. Chem. Phys. Discuss., https://doi.org/10.5194/acp-2018-780
Manuscript under review for journal Atmos. Chem. Phys.
Discussion started: 30 August 2018

locations (middle column), and pixel fractions of one core within another (right column) are considered. Line colors indicated different core types (see legends), while corresponding shaded color regions indicate the standard deviation. Normalized time enables to average together CCEs with different lifetimes, from formation to dissipation. The number of CCEs averaged together for each simulation is included in the left column panel titles.

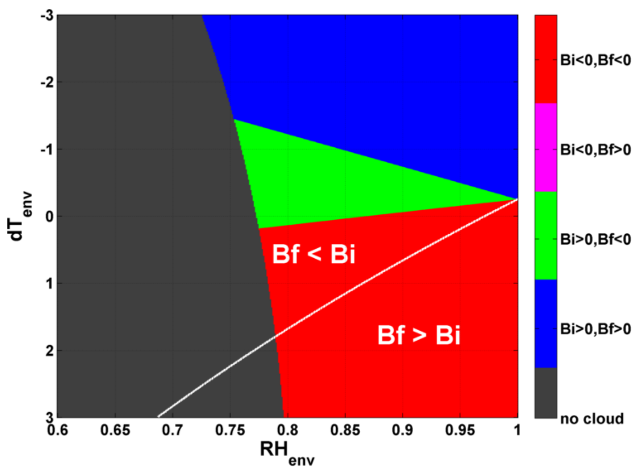

Figure A1. Phase space presenting the effects of entrainment on cloud buoyancy, where the initial cloudy parcel buoyancy (Bi) and final mixed parcel buoyancy (Bf) are considered. A mixing fraction of 0.5 is chosen. The initial cloudy parcel is saturated (S=1), has a temperature of 15^{o}C, pressure of 850 mb, and LWC of 1 g kg^{-1}. The X-axis spans a range of environment relative humidity values (RH_{env}), and the Y-axis a temperature difference ($dT_{env}=T_{env}-T_{cld}$) range between the cloud and the environment parcels. Red color represents B_i <0 & B_f <0 (i.e. parcel stays negatively buoyant after the mixing), magenta represents B_i <0 & B_f >0 (i.e. transition from negative to positive buoyancy), green represents B_i >0 & B_f <0 (i.e. transition from positive to negative buoyancy), and blue represents B_i >0 & B_f >0 (i.e. parcel stays positively buoyant). The grey color represents mixed parcels that were depleted from water (LWC value lower than 0.01 g kg^{-1}) after evaporation, and are considered non-cloudy. The white line separates between areas where B_f > B_i and B_f < B_i.

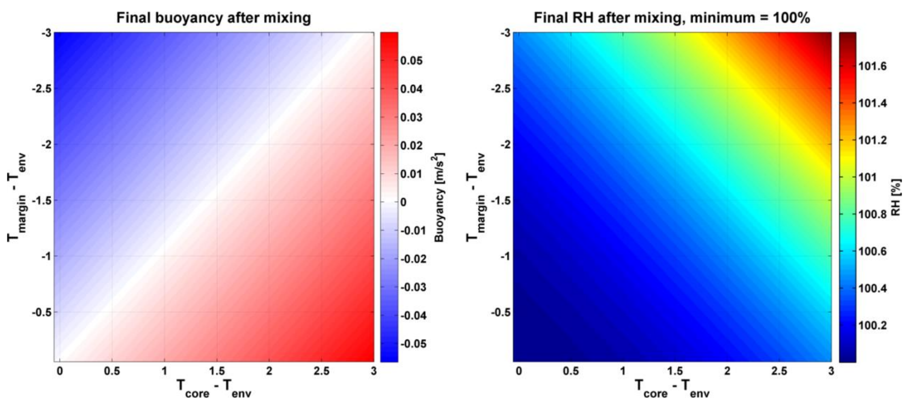

Figure B1. Phase space presenting the resultant buoyancy (left panel) and relative humidity (RH, right panel) when mixing B_{core} and B_{margin} parcels with equal RH but different temperatures. A mixing fraction of 0.5 is chosen. Both parcels are initially saturated (RH=100%), and have a LWC of 0.5 g kg^{-1}. The environment has a temperature of 15^{o}C and pressure of 850 mb. The X(Y)-axis spans the range of temperature differences between the B_{core} (B_{margin}) parcel and the environment.